

Extreme Fast Charge Challenges for Lithium-ion Battery: Variability and Positive Electrode Issues

Author Names: Tanvir R. Tanim^{a,z}, Eric J. Dufek^a, Michael Evans^a, Charles Dickerson^a, Andrew N. Jansen^b, Bryant J. Polzin^b, Alison R. Dunlop^b, Stephen E. Trask^b, Ryan Jackman^a, Ira Bloom^b, Zhenzhen Yang^b, and Eungje Lee^b

Affiliations(s):

^a Idaho National Laboratory, 2525 N. Fremont, Idaho Falls, ID 83415, USA

^b Argonne National Laboratory, 9700 South Cass Avenue, Lemont, IL 60439, USA

^z corresponding author

Abstract

Enabling a 10 min fast charge for electric vehicles is a possible route to reduce range anxiety and increase the utility of electric vehicles. While lithium plating during fast charging is a known challenge, the full suite of limitations which occur in full cells during a 10 min fast charge are unknown. In the present work the central constraints of extreme fast charging are explored through extensive experiments and analysis in single layer graphite/NMC532 pouch cells. Methods of developing fast-charging protocols considering the impedance and transport limitations are presented and the relative benefits of altering the charging rate, profile, relaxation, *etc.*, are investigated. Analysis during and at the end of cycling identified both known and unexpected aging pathways. The most distinct outcomes from the work are a significant increase in cell-to-cell variability as the number of fast charge cycles increase [up to 11% (1σ)] and the identification of distinct aging of the NMC532 positive electrode including cracking of the secondary particles and a trend towards under-lithiation of the positive electrode. While significant aging of the positive electrode was observed, only a few conditions had discernible Li plating and no distinct reversible Li signature was seen during periodic reference performance tests.

Acronyms

BEV	battery electric vehicles
BOL	beginning of life
CC	constant current
CV	constant voltage
de	delithiated
EOC	end of charge
EOD	end of discharge
Gr	Graphite
IC	$dQ.dV^{-1}$
LiPF ₆	lithium hexafluorophosphate
LLI	loss of lithium inventory
LAM	loss of active material
LIB	lithium-ion battery
li	lithiated
NE	negative electrode
N: P ratio	negative to positive capacity ratio
NMC532	$LiNi_{0.5}Mn_{0.3}Co_{0.2}O_2$
OCV	open circuit voltage
OFS	voltage offset
PE	positive electrode
RPT	reference performance test
SEI	solid electrolyte interphase
XFC	extreme fast charging

Introduction

Lithium-ion batteries (LIBs) currently are the battery of choice for electrified vehicle drivetrains.^{1,2} A global effort is underway to identify limitations and enable a 10-minute recharge of battery electric vehicles (BEV).³⁻⁵ Extreme fast charging at rates between 4.8 and 6C that can replace 80% of pack capacity in 10 min is seen as appealing to consumers and as key to widespread adoption of BEVs, which is essential to reduce global greenhouse gas emissions and warming.⁶⁻⁸ Such high rate charging increases the likelihood of problematic Li plating due to the small difference between the potential for Li plating and the operating potential (~ 0.1 V vs. Li/Li⁺) of graphite.⁹ Li plating is problematic when high cycle life is needed as it directly reduces the inventory of Li through the irreversible deposition of Li and additional solid electrolyte interphase (SEI) formation.³ Irreversibly plated Li is electrochemically isolated, and ultimately leads to accelerated capacity fade.^{10,11} Reports also suggest that a fraction of plated Li is electrochemically reversible and can be observed as a distinct high voltage plateau during discharge.¹²⁻¹⁶ While Li plating and impacts to the negative electrode are typically evaluated, there is little information on the impacts of fast charging on the other cell components including the positive electrode.

Most published reports on fast charging are limited up to 4C and based on a variety of commercially available, graphite-based LIBs without revealing key material, electrode, and cell design parameters.^{12, 17-20, 24-27} The lack of design parameters makes it difficult to accurately identify, quantify, and prioritize the critical cell design parameter(s) that would enable extreme fast charging (XFC) in the range of 6C and above. Among the suggested routes to facilitate fast charging are elevated temperature during fast charging,¹⁹⁻²² and the use of different charging

protocols, that vary charging voltage, charging current profile, *etc.*, to retain expected performance and life of the fast charged battery.^{23-26, 28-31}

Due to the lack of specific design parameters it is difficult to obtain a clear understanding of the bottlenecks of fast charging in the range of 6C and above and the benefits of different advanced methods to improve fast charging performance. A concerted effort in understanding the interplay between materials, electrode structure, and use conditions during XFC is essential to resolve the issue. At the same time, developing a more refined analysis and characterization of degradation mechanisms including loss of lithium inventory, plating of lithium and loss of active material from both electrodes using realistic techniques are vital to enable fast charging of specific energy cells.

Using well defined cells, this paper presents the impacts of XFC (up to 9C and 10 min) on graphite/NMC532 single layer pouch cells. Single layer pouch cell serves as a controlled unit cell to identify the primary scientific bottlenecks of XFC minimizing the secondary effects of temperature, which could be mitigated by adequate engineering design in full cell settings. The work systematically looked at several different charging protocols, which were developed based on the rate performance for this specific cell design. The impact of these charge protocols was evaluated to more precisely identify key gaps which may emerge with XFC. Of note is that this study has identified distinct issues which arise with cell variability as aging occurs and has also found key issues with positive electrode performance and degradation during fast charging. These issues are often overlooked due to the focus on Li metal plating during fast charging, but have the potential to significantly impact the eventual application and use of fast charging.

Experimental

Table I lists the material, electrode, cell design parameters, and Table II includes the charging protocols. Graphite (1506T Superior Graphite) and NMC532 (Toda America) were used as respective negative and positive electrode active materials, respectively, to fabricate electrodes at the Cell Analysis, Modeling, and Prototyping (CAMP) Facility at Argonne National Laboratory (Argonne). These electrodes were cut and assembled in single layer pouch cells with Celgard 2320 separator. 1.2 M LiPF₆ in a 3:7 by wt. ethylene carbonate: ethylmethyl carbonate electrolyte was used. The reversible capacity of the negative electrode and positive electrode at C/10 were measured to be 1.93 mAh cm⁻² and 1.65 mAh cm⁻² using half cells. The reversible negative to positive capacity ratio (N: P ratio) was set at 1.17 for C/10 rate (1.26 for C/1) by adjusting the mass loading of the electrodes for the operating cell voltage window of 3-4.1V. The cells were built such that the footprint of the negative electrode overhung the edge of the positive electrode by 0.5 mm on all sides. Such oversize accommodates slight imperfections of electrode alignment during cell assembly and avoid preferential plating of Li at the edges by guaranteeing there is Gr material directly opposite of the cathode.^{32,33} Single-sided electrodes were used in an xx3450 pouch cell format with an active area of 14.1 cm² for the positive electrode and 14.9 cm² for the negative electrode.

Twenty-one cells were assembled in a dry room and formed at CAMP prior to shipment to Idaho National Laboratory (INL) for life and performance evaluation and failure mode analysis. Upon receipt, mass, open circuit voltage (OCV), and high frequency impedance of the cells were measured. Supplemental Figs. A-1(a)-(c) show the experimental setup and fixturing details. The cells were sandwiched on one side with 6.35 mm thick rectangular Lexan block to focus the

applied pressure, and on the other side with 6.35 mm thick polypropylene sheet. The Lexan and polypropylene sheets were then sandwiched on each side by 6.35 mm thick stainless-steel plates using springs which were uniformly tightened such that they provided 15-30 kPa pressure. A single thermocouple (Omega 5SC-TT-T-30-36, Type T) was placed [Fig. A-1(c)] near the positive electrode about 13 mm below the tab edge to measure the cell temperature during testing.

Following fixturing, electrochemical evaluation of the cells was performed at $30 \pm 1^\circ\text{C}$ in an environmentally controlled chamber (TestEquity 1007C). A MACCOR series 4000 Automated Test System was used for cycling while a Solartron 1287 potentiostat and Analyzer model 1260 were used for electrochemical impedance spectroscopy (EIS) measurements. Initial cycling to understand as received cell variability consisted of multiple constant current (CC) rates (C/20 and C/1) and EIS tests. Cells were charged at C/20 or C/1 to V_{max} (4.1V) followed by a 1h rest before starting the C/20 or C/1 CC discharge tests, respectively.^{34,35} Cells were charged to 3.8V at C/1 and rested for 15 min before taking EIS measurements. EIS measurement was performed with 10 mV RMS voltage over 500kHz to 1 mHz.

Rate capability tests were performed at constant C-rates (1C through 9C, without any constant voltage step) on three cells (1-3). All C-rates were based on the measured discharge capacity for each cell at 1C at BOL. Six, 10-min charging protocols were then developed based on the rate capability test performance (see Table II). Three cells were used for each of the developed protocols, which included a 15 min rest after a 10-min charging step [Fig. A-1(d)]. Following the post-charge rest, a C/2 discharge and an additional 15 min rest were conducted before the next charge. Reference performance tests (RPT) occurred at specific cycling intervals,

which included a C/20 charge-discharge with 1h rest in between, C/1 discharge test and electrochemical impedance spectroscopy (EIS) tests at 3.8V as described above.

Analysis of aging was performed using a $dQ.dV^{-1}$ method developed by Dubarry et al.³⁴ They later implemented the mechanistic approach in a Matlab-based simulation toolbox named “Alawa”.³⁶ Alawa emulates any one or combinations of the five aging modes mentioned earlier. Comparing emulation with experimental $dQ.dV^{-1}$ evolution helps isolate the aging pathway for a specific cell or condition. Quantification is possible by combining the identified aging modes to different degrees and evaluating against the experimental $dQ.dV^{-1}$. In addition to half-cell data mentioned above for graphite and NMC532, Alawa takes into account and provides information on how the N: P ratio and voltage offset (OFS), which arises due to SEI formation, change as a function of aging. More details on this mechanistic approach can be found in ref^{27, 34}.

After completion of electrochemical testing, all the cells were disassembled in a Ar-filled glove box after discharging to 3V at C/2 followed by a 2h voltage hold. The cycled positive electrodes were washed two times with excess dimethyl carbonate (1 min each) and dried in the glove box at room temperature. The dried samples were then sealed in Kapton film for ex-situ XRD measurements (Bruker D8 Advance). Lattice parameters were calculated by Le Bail fitting method using TOPAS software package. The sample height error was corrected based on the peak position of Al current collector.

Electrode morphology after cycling was examined by Scanning electron microscope (Hitachi S- 4700) at 10KV. The cross section of the electrodes were obtained using an Ar+ ion beam milling system (JEOL, IB-09010 Cross section polisher).

<Table I>

<Table II>

< Supplemental Fig. A-1 >

Results

1) Initial characterization and fast charge protocol development

Upon receipt, cells were characterized using OCV ($3.51 \pm 0.01 \text{V}$, 0.22%), high-frequency impedance at 1 kHz ($0.55 \pm 0.02 \Omega$, 3.6%), mass (2.33 g, 0.97% 1σ variability), and discharge capacity measured at C/20 and C/1 to be 22 mAh and 19 mAh with less than 2% variability (1σ). A rate capability test was performed on a subset of cells [Fig. 1(a), cells 1-3] to evaluate impedance and transport limitations and to aid in protocol development. Charge acceptance linearly decreased with C-rates (*e.g.*, 100% at 1C, 86% at 5C and 66% at 9C) due to higher polarization. The V_{\max} (4.1V) is reached before 10 min at C-rates higher than 5C, indicating charging could be continued by modifying the charge protocol or through the use of a constant voltage step. During the fast charging up to 9C, an insignificant increase in cell temperature was measured. Therefore, the effect of temperature is largely be seen as de-convoluted from the electrochemical processes during fast charging, thus helping to identify the true scientific limitations of fast charging.³¹

Two overvoltage parameters were extracted at the end of charge to examine the extent of cell polarization at different charging rates.³⁸ They are impedance overpotential, ΔV_{imp} =immediate relaxation in voltage at the end of charge and transport polarization, ΔV_{trans} =the difference in voltage between the immediately relaxed state and after 15-min rest, a pseudo-equilibrium state [see Fig. 1(a)]. The impedance overvoltage includes the Ohmic and reaction kinetic overvoltages and the transport overvoltage is primarily impacted by Li^+ transport in both the liquid and solids of the battery.³⁸⁻³⁹ Figure 1(b) summarizes the impedance and transport

overvoltages as a function of C-rate, which shows that transport overvoltage dominated the overall voltage loss with a distinct increase above 7C. Impedance voltage loss increases linearly with C-rate all the way up to 9C. Electrolyte concentration change at the positive electrode and negative electrode as well as particle surface saturation by Li^+ in the positive electrode and/or depletion in the negative electrode, respectively, could contribute in exacerbating the transport overvoltage above 7C rate.³⁹ Two C-rates were chosen as the basis for the suite of charging profiles to ensure the cells were in aggressive fast charging scenarios: one at 6.8C (below the 7C transition point) and the other one at 9C. These rates were distinctly chosen to better understand the impact of Li^+ transport on cell aging. Additionally, the 9C conditions imitate a boost charging protocol, reported as an alternative option for fast charging.²⁵

<Figure 1>

Transport polarization, such as what is seen in Fig. 1, can be relaxed by altering current or adding rest time when severe transport limitations arise. Adding a CV step where current tapers off at a particular upper cut-off voltage is a common example.²⁴ Stepping the current down to a lower value when the maximum voltage is reached is another possibility.²⁸⁻²⁹ The inclusion of rest time during fast charging has also been investigated to relax transport limitations.²⁵ These three routes were considered for the design of six, 10-min charging protocols:

- (i) Constant current-constant voltage (CC-CV) charging at 6.8C and 9C: Charge at 6.8C or 9C until V_{\max} is reached then switch to CV charging at V_{\max} until the total time reaches 10 min.
- (ii) Two-step constant current charging protocol at 6.8C and 9C: Charge at either 6.8C or 9C until V_{\max} is reached. Once V_{\max} is reached, continue charging at a lower rate until total charging time reaches 10 min. The lower rate is the theoretical rate required to fully charge the battery

within the time left after hitting V_{\max} . For the 6.8C initial rate the lower rate equated to 3.25C, and 3.5C equated to the second rate for the 9C condition. If V_{\max} was reached during the lower rate of charging (prior to 10 min), a CV mode was used until the full 10 min charging time was reached.

(iii) Pulse charging protocol: Rest 17.65 s after every 20% recharge capacity (based on BOL C/1 capacity) while charging at either 6.8C or 9C. CV charging step triggered when V_{\max} is reached (usually the last pulse). Total charging time was maintained at 10 min.

Supplemental Fig. A-2(a) shows the three versions of the current profiles at 6.8C at BOL as an example. Regardless of the different protocols, a CV component was necessary to finish the 10 min charge. The 6.8C protocols had an RMS current of 5.8C. For the 9C protocols, RMS currents slightly varied: 6.4C for CC-CV, 6.3C for the 2-step and 6.5C for the pulse profile.

Presented in Figure 1(c) are the charge acceptances at BOL for the six charging protocols. Each protocol replaced at least 90% of the BOL C/1 capacity. However, the charge accepted during the CV portion of the protocol [Fig. 1(c)] varied. The 2-step current profiles respectively had the least charge accepted during CV.

< Supplemental Fig. A-2 >

2) Aging Analysis

Reference performance tests were included in the testing regime to quantify aging. The percent capacity fade from the RPTs referenced against the BOL C/20 capacity is shown in Fig. 2. As with the rate capability test no discernable temperature increase was detected as the cells aged. This is not unexpected as the maximum I^2R heat at 9C was estimated to be 16 mW. While no temperature increase was noted, a significant increase in cell-to-cell variability arose in most

groups with the pulse charging procedure showing the maximum variability for both 6.8 and 9C [Figs.2(c) and (f)]. Variability in performance started from the beginning of cycling with clear distinction within 100 cycles. Careful examination of Fig. 2 shows cells that aged 8-10% over 400 cycles displayed a close to linear fade while the cells with higher percent fade aged in a non-linear fashion.

<Fig. 2>

2.1) Understating impedance and transport evolution with aging

<Fig. 3>

The CC rate capability test was repeated at the completion of cycling (after 400 fast charge cycles) to examine the evolution of impedance and transport polarizations with aging. The C-rate of the individual cell was adjusted based on their respective C/1 capacity after 400 cycles to ensure the same effective C-rate as the BOL test. Figure 3(a) overlays the average overpotentials for impedance and transport for each charge protocol group and the BOL overpotentials from Fig. 1(b). Despite the variation in capacity fade no change in transport overvoltage can be observed suggesting the bulk transport properties of the solid and liquid phases were not impacted by fast charging. An overall increase in impedance voltage loss (ΔV_{imp}), which lumps both Ohmic and interfacial resistances, is noticeable without a clear correlation with charging rate, protocol or capacity fade.

To better differentiate the Ohmic and interfacial resistances, EIS tests were performed on all individual cells [Figs. 3(b)-(c)]. As expected, due to the low variability at BOL, no significant variation in EIS spectra is noticed at the BOL. The Nyquist plots from cells 4-6 are included in Fig. 3(b). Figure 3(c) includes representative spectrum for each condition following aging. Comparison of Figs. 3 (b) and (c) shows a minor increase in Ohmic resistance (R_{ohm}) after 400

cycles irrespective of the extent of aging. For instance, for the 6.8C protocols ΔR_{ohm} remains between 0.046 to 0.049 Ω and for the 9C protocols $\Delta R_{ohm} = 0.043 - 0.057\Omega$. Ohmic resistance is primarily dictated by the electronic resistance of the solid phases (both positive and negative electrodes) and ionic resistance of the electrolyte. A minor increase in Ohmic resistance indicates that the electronic and ionic pathways remained relatively unchanged throughout the fast charge cycling. Moreover, the ionic conductivity of the electrolyte is a few orders lower than the electronic conductivity.³⁹⁻⁴⁰ Thus, a significant amount of loss of active material (LAM) would need to occur to manifest as an increase in Ohmic resistance. Thus, the minor increase in Ohmic resistance could primarily be attributed to the electrolyte associated with solvent and/or salt reduction.

While R_{ohm} was largely unchanged, a significant (nearly double) increase in interfacial impedance is noticeable in all the cells [Fig. 3(a)]. Each of the cells, regardless of the extent of capacity fade, displayed the large increase in interfacial impedance though to different extents which did not directly correlate with percent capacity fade. Thus, the increase in impedance voltage loss (ΔV_{imp}) in Fig. 3(a) can primarily be linked to the growth of the interphase layer and sluggish electrode reaction kinetics.

2.2) Understanding the origins of aging

Figures 4(a)-(d) show side-by-side comparison of the voltage and incremental capacity ($dQ \cdot dV^{-1}$) as the number of fast charge cycles increased for cell 15, 9C CC-CV (8% fade, the lowest aged cell) and cell 19, 9C pulse (32% fade, one of the highest aged cells). The dominant $dQ \cdot dV^{-1}$ peaks relate to distinct phase changes that occur in the graphite and NMC electrodes. The three most prominent peaks, identified as I, II, and III in Fig. 4(b) are primarily associated

with different stages of graphite lithiation though they are convoluted by NMC transitions in the same voltage window. Details on peak indexing are shown in supplemental Fig. A-3 using identical graphite and NMC532 data collected in CR2032 half-cells.

Qualitatively, a minor decrease in peak intensity for all the peaks can be seen in the cell 15 (8% fade). Cell 19 (32% fade), however, displays a significant and non-uniform reduction in peak intensity, *i.e.*, a minor decrease in peak I but a considerable decrease in peak II and III. A decrease in peak intensity could either be associated to LAM in the negative electrode (NE) or loss of lithium inventory (LLI) due to SEI formation on the NE or both.^{27,34} However, LAM in the NE would have translated into a uniform decrease in intensity for peaks I, II and III associated with graphite utilization. Thus, a disproportionate reduction in peak intensity in the higher aged cell cannot be attributed to LAM in the NE, and points towards LLI as one of the dominating aging modes. Peak broadening is another notable feature in the $dQ.dV^{-1}$ plots [Figs. 4(b) and 4(d)]. The most pronounced being peak III, which became almost flat near the end of cycling. This could be attributed to increased N: P ratio, possibly due to LAM in the positive electrode (PE).

<Fig. 4>

Quantitative $dQ.dV^{-1}$ analysis provides the opportunity to quantify aging modes with increased confidence. Broadly LIBs experience five dominant aging modes: LAM in the PE in the lithiated (LAM_{LiPE}) and delithiated (LAM_{dePE}) states, LAM in the NE in the lithiated (LAM_{LiNE}) and delithiated (LAM_{deNE}) states and LLI in the NE SEI, *e.g.*, irreversible Li lost in side reactions and/or isolated dead Li followed by Li plating.³⁹⁻⁴⁰ Each of these different aging modes manifest as different $dQ.dV^{-1}$ signatures with aging. Using the distinct signatures related to each mode of aging with the experimentally calculated $dQ.dV^{-1}$ signatures [Figs. A-4(b) and

A-4(d)] and the combined EOC and EOD rest voltages as shown in Fig. 4(e) enables identification of the dominate aging modes.

< Supplemental Fig. A-3>

The C/20 emulated voltage and corresponding $dQ.dV^{-1}$ signatures at different aging states and the expected trend of EOC and EOD voltages for the five aging modes are shown in Fig. A-4. For the NE, as previously discussed, the $dQ.dV^{-1}$ signatures and experimental EOC and EOD in Fig. 4(e) do not match with LAM_{deNE} , removing it from consideration as a dominate aging mode. For the PE, the rest voltage after charging did not increase indicating the cells did not over de-lithiate as a function of aging [Fig. A-4(e)] thus removing LAM_{HiPE} from consideration as a dominating aging mode. The decreasing trend of EOD rest voltage and $dQ.dV^{-1}$ evolution with aging closely matches LAM_{dePE} . Thus, in addition to LLI, LAM_{dePE} is a primary aging mode indicating a significant positive electrode material loss as a result of extensive fast charging

< Supplemental Fig. A-4>

With the two dominant aging modes identified, the extent of LLI and LAM_{dePE} were quantified. In Fig. 5, the cell 15 (8% fade) and cell 19 (32% fade) are highlighted. The fraction of aging modes shown in Figs. 5(d) and (j) are the result of Alawa refinement where the same respective total percent fade from experiment and emulation [Figs. 5(e) and 5(k)] align while also generating comparable $dQ.dV^{-1}$ signatures in Figs. 5(a)-(c) and (g) –(i). Comparable $dQ.dV^{-1}$ signatures between Alawa and experiments can be seen at cycle 0 (BOL), 175 and 400 for cell 15. For cell 19, which had enhanced fade, the overall trend in $dQ.dV^{-1}$ holds but some discrepancies, especially, towards the end of cycling can be observed. This is probably due to the alteration of the positive electrode open circuit potential with aging that resulted from sluggish

interphase kinetics. Note that Alawa uses the BOL slow rate data throughout the simulation without incorporating changes in kinetics.

Alawa was also used to calculate the OFS and N:P ratios with aging as shown in Fig. 5(f) and (l), providing pertinent information on the progression of cell balance with aging. Both the LAM_{dePE} and LLI trend linearly throughout cycling for cell 15 resulting in linear capacity fade. For cell 19 the rate of LAM_{dePE} and LLI, decreased slightly towards the end of cycling resulting in a reduced overall capacity fade rate. Similar behaviour was observed in cells 6, 17, and 20 (results not shown). For all the cells, as highlighted in Fig. 5, LAM_{dePE} occurred at a rate which exceeded LLI, indicating the emergence of severe positive electrode degradation during fast charge cycling. As a result, cell balance was altered significantly, *i.e.*, a decrease in OFS and an increase in N:P ratio were observed. Towards the end of cycling, the OFS became negative. A positive OFS means that the negative electrode voltage limits the cell discharge capacity and a negative OFS indicates that the positive electrode voltage limits the discharge capacity (see supplemental Fig. A-4). In the present case the reduction in OFS suggests that as aging progressed the positive electrode was driven to a lower voltage during discharge in agreement with the EOD rest voltage in Fig. 4(e).

<Fig 5>

Despite the 15% positive electrode active material loss after 400 fast charge cycles, cell 15 manifests only 8% capacity loss [Fig. 5(d) and Fig. A-5(a)]. During formation at the BOL a 7% voltage OFS (an inherent behaviour of graphite-based LIB) masked the additional 7% positive electrode capacity fade at the end of the fast charge cycling. Thus, during the early stages of fade aging due to LAM_{dePE} was a silent aging mode that wasn't evident as capacity fade

until the OFS became negative. Cell 19 followed a similar trend but at an elevated rate [Figs. A-5(j) and A-5(b)].

< Supplemental Fig. A-5 >

3.3.3 Post-test analysis

Following cycling, selected pouch cells from each group were disassembled in an argon-filled glove box after discharging them to 3.0V. Optical images of the selected anodes from each group are shown in Figs. 6(a)-(g). Overall, no conclusive visual sign of Li plating was observed for the 6.8C groups [Figs. 6(a)-(c)] suggesting SEI was the dominant component of LLI. Some of the cells with more extensive aging from the 9C fast charging groups showed obvious signs of Li plating (cell 13, 18% capacity fade and cell 19, 32% capacity fade). The 9C pulse charging group displayed the most distinct signs of Li plating. Of the 9C charging protocols the 2-step group displayed no visual indication of Li plating as represented by cell 17 which had the most capacity fade within the group [Fig. 6(e)].

Figure 6(h) shows the half-cell C/20 $dQ.dV^{-1}$ comparison of an unaged positive electrode sample after formation and harvested positive electrodes from cells 15 and 19. Significant reduction in peak intensity is seen, along with peak broadening verifying the PE LAM $dQ.dV^{-1}$ analysis. The extent of experimental capacity fade *e.g.*, 16% for cell 15 and 39% for cell 19, compares well with the quantitative $dQ.dV^{-1}$ analysis presented earlier. The slightly reduced $dQ.dV^{-1}$ value in the higher voltage, solid solution region above 3.9V, is likely due to slightly reduced utilization of the NMC.

<Fig. 6>

SEM images in Figs. 7(a)-(b) show that NMC532 secondary particles cycled at 6.8C better maintained their original integrity though some cracks are clearly visible. Positive electrodes cycled at 9C show more intergranular cracking compared to the ones cycled at 6.8C. For the 9C CC-CV cases shown in Figs. 7(d)-(f), the shape of NMC532 particles is still retained, but distinct cracking between primary particles is visible. Such cracking is expected to result in poor grain-to-grain connections and primary particle isolation. The presence of particle cracking was confirmed in other positive electrodes cycled at 9C.

<Fig. 7>

<Fig. 8>

<Table III>

Figure 8 compares the ex-situ X-ray Diffraction (XRD) for samples from a pristine NMC532, cell 5 (6.8C CC-CV) and cell 13 (9C CC-CV), as representative cases. The Miller indices were identified from ref. ⁴¹⁻⁴² The pristine sample has a higher c/a ratio (>4.899) and distinct splitting of diffraction peaks (006)/(012) and (018)/(110), indicative of well-defined hexagonal layered structure. ⁴³⁻⁴⁴ The integral intensity ratio, $I_{(003)}/I_{(104)}$, of the pristine sample is larger than 1.2, an indication of no cation disordering or mixing between lithium and bivalent nickel ions in the crystal structure. ⁴³⁻⁴⁶

A decreasing trend in the overall peak intensity at all reflection angles suggests the positive electrode lost active material during fast charge cycling, in-line with our previous analysis and observations. No new reflection peaks are visible indicating no new phases form during cycling. ⁴³ However, the lattice parameters of the unit cells of the cycled positive electrodes change as compared to that of the pristine material. Specifically, the c-axis has

expanded and the a-axis, contracted, as shown in Table III. This trend is attributed to the positive electrode being in a slightly under-lithiated state towards the end of cell discharge.^{41, 47} The XRD data is in line with our previous observations of accelerated LAM_{dePE}. Despite the changes in the c and a-axes, the $I_{(003)}/I_{(104)}$ intensity ratio remains well above 1.2, indicating minimum cation disordering after significant fast charging.

Discussion

The charging performances and related aging trends observed in this study provide distinct insight into key challenges associated with XFC. First, straight evaluation of fast charge protocols requires that the key design parameters (Table I and II) and the respective rate capability of the cell are known (Fig. 1). A valuable method to understand the cell limitations is to understand the cell overpotential at different rates. For the present cells, the change in transport observed at 7C served as a distinguishing point. Charging at rates higher than 7C, while keeping the time constant at 10 min, did little to increase the overall charge acceptance. Indeed, when charging at 9C only 2-5% additional charge was accepted. This marginal benefit does not justify the need to charge at higher rates (9C in this case), which would increase the likelihood of Li plating. It also suggests that initial high rate charging (*e.g.*, boost charging) may exacerbate aging. The use of overpotential analysis to develop non-CC-CV charge protocols, was successful in altering the fraction of time in the CC and CV portions of the profile. Of the generated protocols, the use of multiple currents such as in the 2-step profiles provides the most distinct reduction in overvoltage at the end of the 10 min fast charge sequences (supplemental Fig. A-6). Thus over the course of the 10-min profile the reduction in current generated a more uniform Li⁺ concentration gradient across the cell than periods of rest.

The second distinct outcome from this study is that successful demonstration of fast charging at the pack level will require very precise understanding of how a charging profile minimizes or exacerbates cell-to-cell variability. For the cells investigated, despite the low beginning of life variability which was below 2%, the final distribution of capacity fade across the cells ranged from 8 to 38%. This degree of variability is likely to create battery pack management issues and may ultimately lead to fade rates, at the pack level, which exceed what is observed when testing individual cells.²⁷ Identifying the appropriate charge profiles which minimize variability, such as the 2-step profile, will ease pack design and minimize management issues.

While the extent of aging progressed differently for each cell, the basic modes of failure followed the same trend regardless of charge protocol (Figs. 4 and 5). Other recent work looking at variability came to a similar conclusion.⁴⁸ For the current work, LAM_{dePE} consistently dominated LLI in all cases (Figs. 5, A-5 and 6), which altered the cell balance significantly, *i.e.*, reduced voltage OFS and increased N:P ratios. While the modes of aging remained the same for all cells, those that experienced a non-linear capacity fade displayed voltage OFS that became negative during the course of cycling.

During early cycling, based on the positive OFS, the negative electrode dictated the voltage profile and ultimately when the cell reached voltage limits. The OFS masked early fade from the PE. Note that, cells that diverged in capacity fade within a group did not suddenly deviate during cycling; instead, the non-uniform capacity fade started from the very beginning of cycling. Thus the evidence of divergent capacity fade during early cycling suggests that the negative electrode was a key driver in variability. Due to the high rates used for the present study, such variability likely arises from electrode level variability that drive non-uniform aging

by creating local variation in polarization and current density. Such local variation could be originated from the crystal anisotropy, particle to particle contact, spatial differences in composition, porosity, tortuosity, coating weight, and electrolyte wetting, etc.⁴⁹⁻⁵¹ Evidence of electrode level variability can be observed in the post-test optical images which show localized rather than uniform Li plating [Figs. 6(d) and 6(g)]. Further evidence of electrode level variation can be drawn comparing cells 13 and 15 [Fig. 2(d) and Figs. 6(d) and 6(e)]. During the first RPT the cells did not display significant difference in capacity or impedance. However, upon completion of cycling, post-test imaging confirmed irreversibly plated Li on cell 13 (18% fade), but not on cell 15 (8% fade). While other cells (*i.e.* cell 11) with advanced capacity fade did not clearly show optical evidence of Li plating, the increased level of LLI suggests that Li was plated on the negative electrode and subsequently reacted with electrolyte to form excess SEI or became electronically isolated and was thus electrochemically irreversible. The presence of irreversibly plated Li is supported by the electrochemical data which did not show overt signs of reversible Li plating such as a high voltage plateau or a $dQ.dV^{-1}$ peak for both the C/20 discharge during the RPT or the C/2 discharge profiles which immediately followed a fast charge [Fig. 4(c)-(d)]. This result aligns with a recent report showing that direct detection using $dQ.dV^{-1}$ can be complicated.¹⁶

A key observation from this study is the severe loss of PE active material during fast charge cycling [see Figs. 5, A-5 and 6(h)]. The losses can be readily assigned to cracking in the secondary particles as shown in Fig. 7 and incomplete lithiation at the end of cell discharge. However, the PE crystal structure remained intact without any firm indication of cation (Ni^{2+} and Li^{+}) disordering, regardless of the two charging rates (see Fig. 8 and Table III). Thus, the reduced capacity of the PE cannot be attributed to the change in structural phases.⁴¹⁻⁴² The

retention of secondary structure in the PE at 6.8C is additional support for the need to understand cell rate capability and overvoltages [Fig. 1(b)].

Most studies in the literature report PE particle cracking due to diffusion-induced stress during high rate insertion during cell discharge.⁵²⁻⁵⁷ This study builds on those findings by linking high rate charging with cracking and fragmentation of PE particles during high rate Li extraction. Heterogeneous concentration gradients in the PE particles during high rate charging likely created non-uniform stress fields which generated voids and ultimately cracks. As cracking led to particle fragmentation and isolation, which would result in under lithiation at the end of discharge and appear electrochemically as loss of PE active material.

< Fig. A-6 >

Conclusion

This study identified some of the constraints for 10 min (6C and above) fast charging for a well-defined Gr/NMC532 Li-ion pouch cell. The study underlines the importance of knowing the key cell design parameters and the respective rate capability while designing and evaluating any fast charging protocol. The overpotential-based approach is a simple, yet powerful method of understanding impedance and transport limits and could guide designing proper charging protocols which minimize degradation. While variability increased across most of the fast charge protocols, the use of reduced current after reaching V_{\max} was found to reduce the extent of aging and variability both of which are vital in battery electric vehicles pack management.

The study finds that loss of active material in the positive electrode, specifically cracking of secondary particles is also a distinct need that needs to be addressed to facilitate fast charging. Both the positive and negative electrodes' fade are exacerbated when charging occurs at rates

where higher transport limited overpotentials are observed. While considering higher energy cell designs future work will need to address cell fade mechanisms at both the negative and positive electrodes to enable fast charging.

This study also identified issues with cell variability and the ability to fast charge. Based on electrochemical and post test data, non-uniformity in aging highlights that attention needs to be paid to uniformity when fast charge conditions are expected. This includes tight control of composition, porosity, tortuosity and overall electrode structure. Distinct heterogeneity may act as a catalyst for Li plating, and ultimately reduced cycle life and increase cell-to-cell variability, during fast charging.

Acknowledgment

Funding was provided from the Vehicle Technologies Office of the U.S. Department of Energy's Office of Energy Efficiency and Renewable Energy under the guidance of the Advanced Battery Cell Research Program (eXtreme fast charge Cell Evaluation of Lithium-ion batteries, XCEL). This manuscript has been authored by Battelle Energy Alliance, LLC under Contract No. AC07-05ID14517 for Idaho National Laboratory with the U.S. Department of Energy, and by Argonne National Laboratory, which is a U.S. Department of Energy Office of Science Laboratory operated by UChicago Argonne, LLC under Contract No. DE-AC02-06CH11357.

The United States Government retains and the publisher, by accepting the article for publication, acknowledges that the United States Government retains a non-exclusive, paid-up, irrevocable, worldwide license to publish or reproduce the published form of this manuscript, or allow others to do so, for United States Government purposes.

The authors thank Samuel Gillard and Peter Faguy from the U.S. Department of Energy for supporting this project. The authors also acknowledge Boryann Liaw for his constructive suggestions in performing the incremental capacity analysis.

Appendix

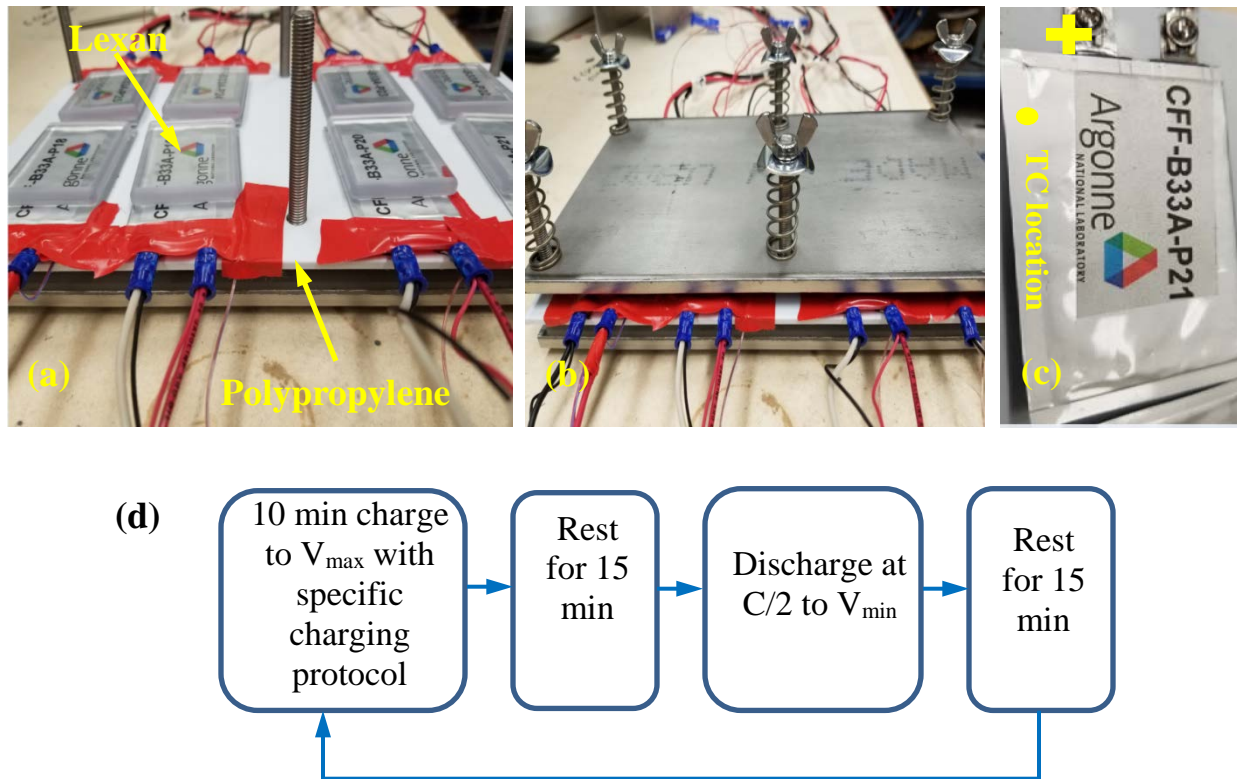


Fig. A-1: (a)-(c) Experimental setup and (d) cycling protocol

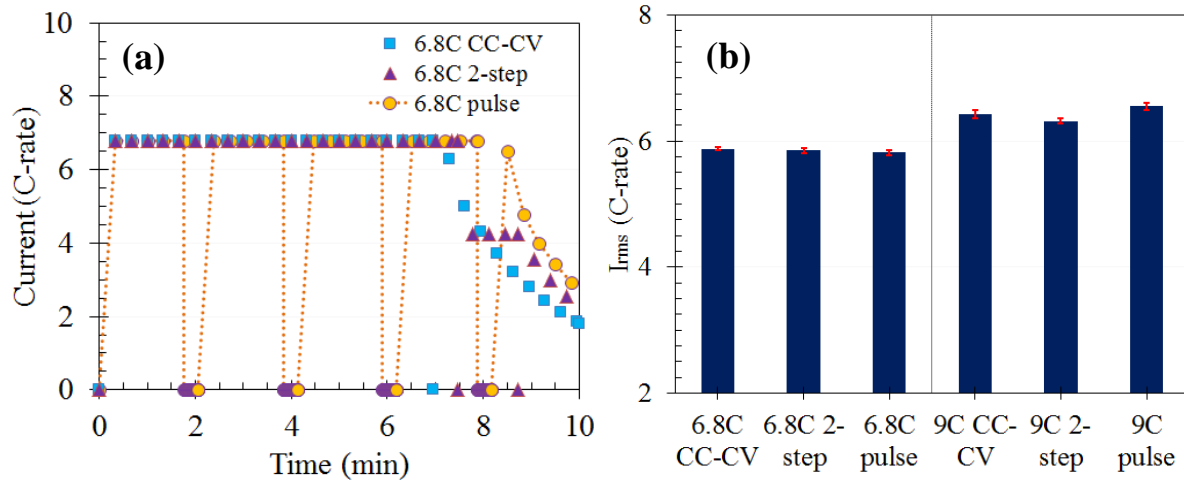


Fig. A-2: (a) Example of 6.8C current profiles at BOL and (b) RMS C-rates of the different current profiles. All C-rates were calculated based on BOL C/1 capacity at 19 mAh.

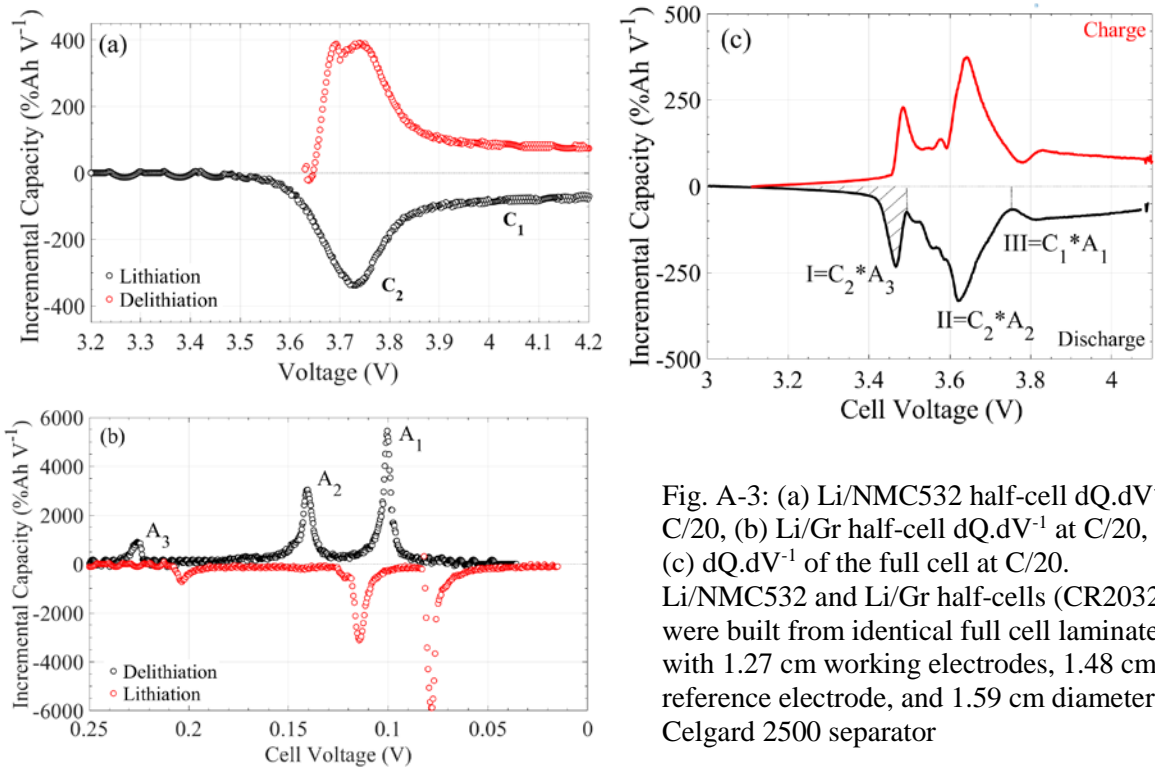


Fig. A-3: (a) Li/NMC532 half-cell $dQ \cdot dV^{-1}$ at C/20, (b) Li/Gr half-cell $dQ \cdot dV^{-1}$ at C/20, and (c) $dQ \cdot dV^{-1}$ of the full cell at C/20. Li/NMC532 and Li/Gr half-cells (CR2032) were built from identical full cell laminates with 1.27 cm working electrodes, 1.48 cm Li reference electrode, and 1.59 cm diameter Celgard 2500 separator

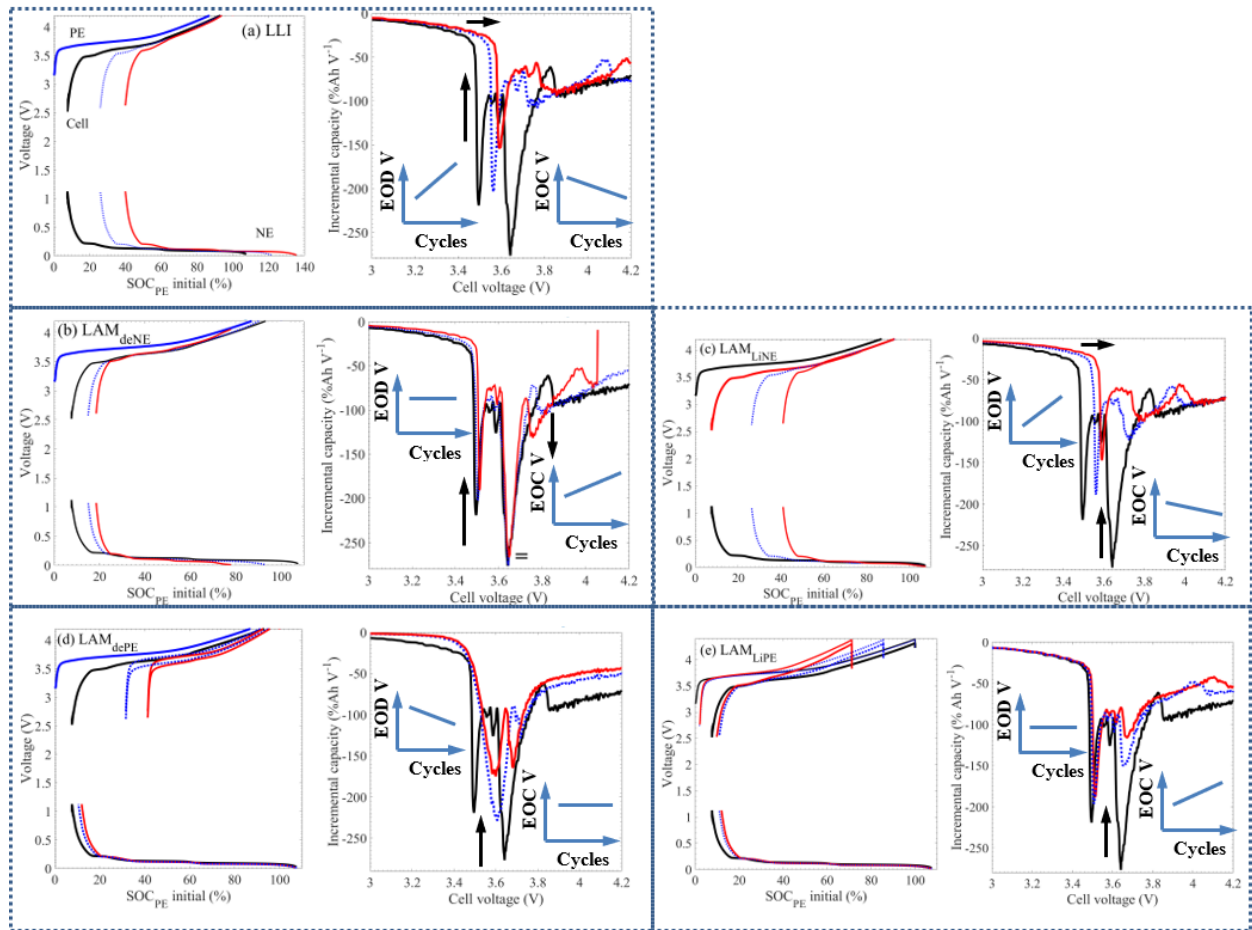


Fig. A-4: Alwa emulation of different aging modes with 7.5% initial offset and N:P=1 for 32% cell capacity fade: (a) 28% LLI, (b) 29.6% LAM_{deNE}, (c) 24% LAM_{LiNE}, (d) 39.2% LAM_{dePE} and 28.7% LAM_{LiPE}

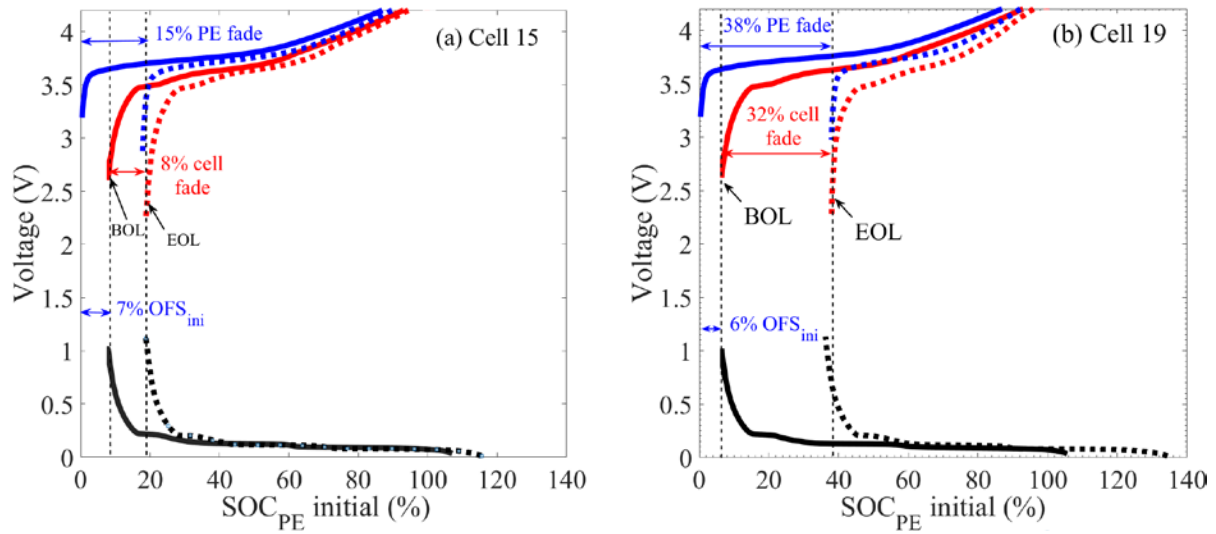


Fig. A-5: Evolution of cell balance (OFS and N:P ratio) with aging: (a) cell 15- one of the lowest aged cells and (b) cell 19- one of the highest aged cells. All simulation performed at C/20 rate. Despite the 15% positive electrode active material loss after 400 cycles, cell 15 manifests only 8% capacity loss. The BOL formation of graphite electrode that resulted in the voltage offset (an inherent nature of gr based LIB) masked the additional 7% positive electrode capacity fade (silent mode of aging). Cell 19 followed a similar trend but at a much-pronounced rate.

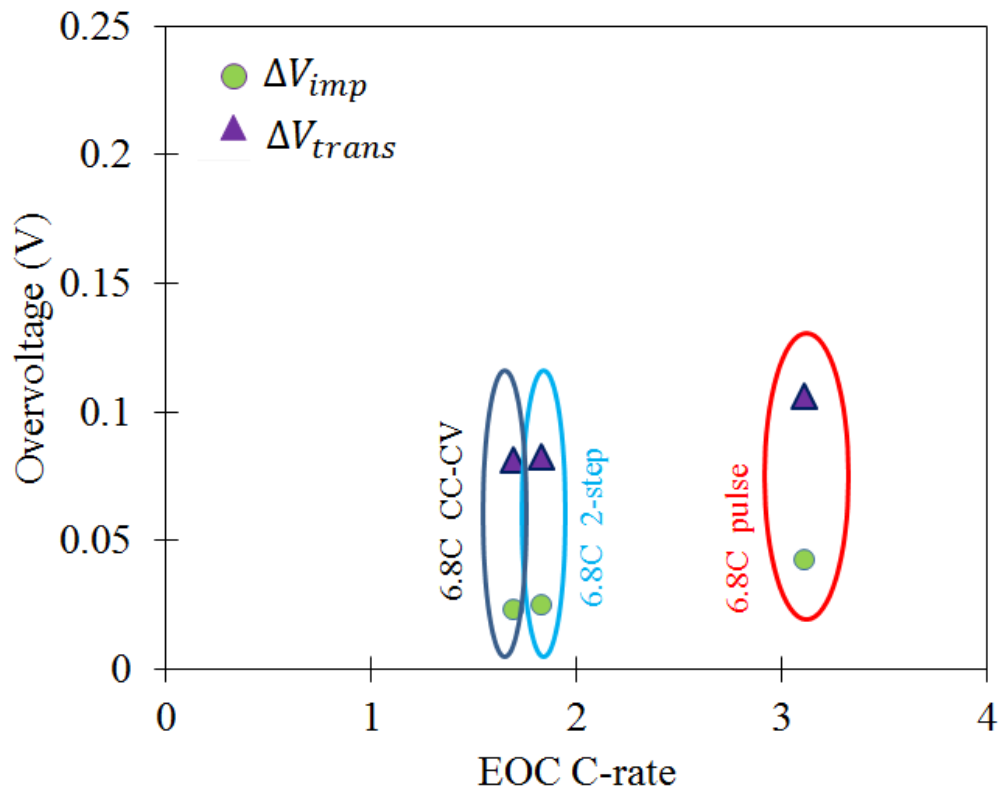


Fig. A-6: Overlaid impedance and transport overvoltages for 6.8C protocols at the end of 1st 10 min fast charge cycle.

References

1. B. Nykvist and M. Nilsson, *Nature Clim. Change*, **5**, 329 (2015).
2. S. M. Knupfer, R. Hensley, P. Hertzke, and P. Schaufuss, McKinsey & Company, Jan 2017.
3. D. Howell et al., *Office of Energy Efficiency and Renewable Energy*, INL/EXT-17-41638 Oct 31 2017.
4. E-Mobility: New Possibilities with 800-volt charging, *Porsche newsroom*,
<https://newsroom.porsche.com/en/technology/porsche-engineering-e-power-electromobility-800-volt-charging-12720.html> (accessed Sep 2017)
5. Charging interface initiative e.V. - Industry statement on future charging infrastructure, available at:
http://www.charinev.org/fileadmin/Downloads/Papers_and_Regulations/CharIN_industry_statement.pdf (accessed June 2017)
6. S. Ahmed et al., *J. Power Sources*, **367**, 250 (2017).
7. N. Lutsey, S. Searle, S. Chambliss, and A. Bandivadekar, *International Council on Clean Transportation*, July 2015
8. M. McCarthy, *Society of Automotive Engineers*, Washington, DC. Jan 2017.
9. V. Schalkwijk and W. Scrosati, *Advances in Lithium-Ion Batteries*, Springer US, 2002
10. K.G. Gallagher et al., *J. Electrochem. Soc.*, **163**, A138 (2016)
11. P. Arora, M. Doyle, and R. E. White, *J. Electrochem. Soc.*, **146**, 3543 (1999).
12. D. Anseán, M. Dubarry, A. Devie, B. Y. Liaw, V. M. García, J. C. Viera, and M. González, *J. Power Sources*, **356**, **36** (2017).
13. C. Kim, K. M. Jeong, K. Kim, and C.-W. Yi, *Electrochimica Acta*, **155**, 431 (2015).
14. R.V. Bugga and M.C. Smart, Lithium plating behavior in lithium-ion cells, *ECS Transactions* **25**, 241 (2010).
15. W. Lu, C. M. L'opez, N. Liu, J. T. Vaughey, A. Jansen, and D. W. Dees, *J. Electrochem. Soc.*, **159**, A566 (2012).
16. I. D. Campbell, M. Marzook, M. Marinescu, and G. J. Offer, *J. Electrochem. Soc.*, **166**, A725 (2019).
17. L. Somerville, J. Bareño, S. Trask, P. Jennings, A. McGordon, C. Lyness, and I. Bloom, *J. Power Sources*, **335**, 189 (2016).
18. A. S. Mussa, M. Klett, M. Behm, G. Lindbergh, and R. W. Lindström, *J. Energy Storage*, **13**, 325 (2017).
19. J. C. Burns, D. A. Stevens, and J. R. Dahn, *J. Electrochem. Soc.*, **162**, A959 (2015).
20. T. Waldmann, B. Hogg, M. Kasper, S. Grolleau, C. Couceiro, K. Trad, B. P. Matadi and M. Wohlfahrt-Mehrens, *J. Electrochem. Soc.*, **163**, A1232 (2016).
21. S. Kim, H. Chen, and H.-Y. S. Huang, *J. Electrochem. En. Conv. Stor.* **16**, 011010 (2019)
22. S. Kim, J. Wee, K. Peters, and H.-Y. S. Huang, *J. Phys. Chem. C*, **122** (2018) 5280
23. C.-K. ChiuHuang, and H.-Y. S. Huang, *J Solid State Electrochem.*, **19** (8) (2015), 2245
24. S. Zhang, *J. Power Sources*, **161**, 1385 (2006).
25. P. Keil and A. Jossen, *J. Energy Storage*, **6**, 125 (2016).
26. Z. Guo, B. Y. Liaw, XQiu, L. Gao, and C. Zhang, *J. Power Sources*, **274**, 957 (2015).

27. T.R. Tanim, M. G. Shirk, R. L. Bewley, E. J. Dufek, and B. Y. Liaw, *J. Power Sources*, **381**, 56 (2018).
28. T.T. Vo, X. Chen, W. Shen, and A. Kapoor, *J. Power Sources*, **273**, 413 (2015).
29. Y. H. Liu, C. H. Hsieh, and Y.F. Luo, *IEEE Trans. Eng. Conv.*, **26** (2) 2011.
30. D. Anseán, M González, J.C. Viera, V.M. García, C. Blanco, and M. Valledor, *J. Power Sources*, **239**, 9 (2013).
31. B. Koo, J. Yi, D. Lee, C. B. Shin, and S. Park, and *J. Electrochem. Soc.*, **165**, A3674 (2018).
32. M. Tang, P. Albertus, and J. Newman, and *J. Electrochem. Soc.*, **156**, A390 (2009).
33. D. W. Dees, A. N. Jansen, and D. P. Abraham, *J. Power Sources*, **174**, 1001, (2007)
34. M. Dubarry, C. Truchot, B. Y. Liaw, and *J. Power Sources*, **219**, 204 (2012).
35. USABC battery test manual for plug-in hybrid electric vehicles, Rev 3, INL/EXT-14-32849
36. Alawa toolbox, available at: <https://www.soest.hawaii.edu/HNEI/alawa/>.
37. M. Keyser et al., *J. Power Sources*, **367**, 228 (2017).
38. X. Yang, T. Miller, *SAE International*, SAE Technical Paper 2017-01-1204, 2017, doi:10.4271/2017-01-1204.
39. F Jiang and P Peng, *Sci. Rep.*, **6**, 32639 (2016).
40. T. R. Tanim, C. D. Rahn, and C.-Y. Wang, 2014 Am. Control Conf., 141 (2014).
41. J. Choi and A. Manthiram, *J. Electrochem. Soc.*, **152**, A1714 (2005).
42. P. Y. Liao, J. G. Duh, and S. R. Sheen, *J. Electrochem. Soc.*, **152**, A1695 (2005).
43. K.M. Shaju, G.V. S. Rao, and B.V.R Chowdari, *Electrochimica Acta*, **48**, 145 (2002).
44. T. Ohzuku, A. Ueda, M. Nagayama, Y. Iwakoshi, and H. Komori, *Electrochimica Acta*, **38**, 1159 (1993).
45. P.Y. Liao, J.G. Duh, R.S. Sheen, *J. Electrochem. Soc.*, **152**, A1695 (2005).
46. Y. He, Z. Ma, X. Liao, and Y. Jiang, *J. Power Sources*, **163**, 1053 (2007).
47. T. C. Bacha, S. F. Schuster, E. Fleder, J. Müller, M. J. Brand, H. Lormann, A. Jossen, and G. Sxntl, *J. Energy Storage*, **5**, 212 (2016).
48. A. Devie and G. Baure, M. Dubarry, *Energies*, **11**, 1031 (2018).
49. S. J. Harris, E. K. Rahaniand, and V.B. Shenoy, *J. Electrochem. Soc.*, **159**, A1501 (2012)
50. K. Smith et al., *ECS Meeting*, **22** 113645 (2019).
51. A. W. Abboud, E.J. Dufek and B. Liaw, *J. Electrochem. Soc.*, **166**, A667 (2019).
52. C. Lim, B. Yan, L. Yin, and L. Zhu, *Electrochimica Acta*, **75**, 279 (2012).
53. K. Zhao, M. Pharr, J. J. Vlassak, and Z. Suo, *J. Applied Physics*, **108**, 073517-1-6 (2010).
54. G. Li, Z. Zhang, Z. Huang, C. Yang, Z. Zuo, and H. Zhou, *J. Solid State Electrochem.*, **2**, 673 (2017).
55. G. Sun, T. Sui, B. Song, H. Zheng, L Lu, and A. M. Korsunsky, *Extreme Mechanics Letters*, **9**, 449 (2016).
56. G. Liu et al., *J. Electrochem. Soc.*, **165**, A3040 (2018).
57. M. Masmoudi, Z. Moumni and F. Bidault, *J. Electrochem. Soc.*, **166**, A5445 (2019).

Figure and Figure Captions

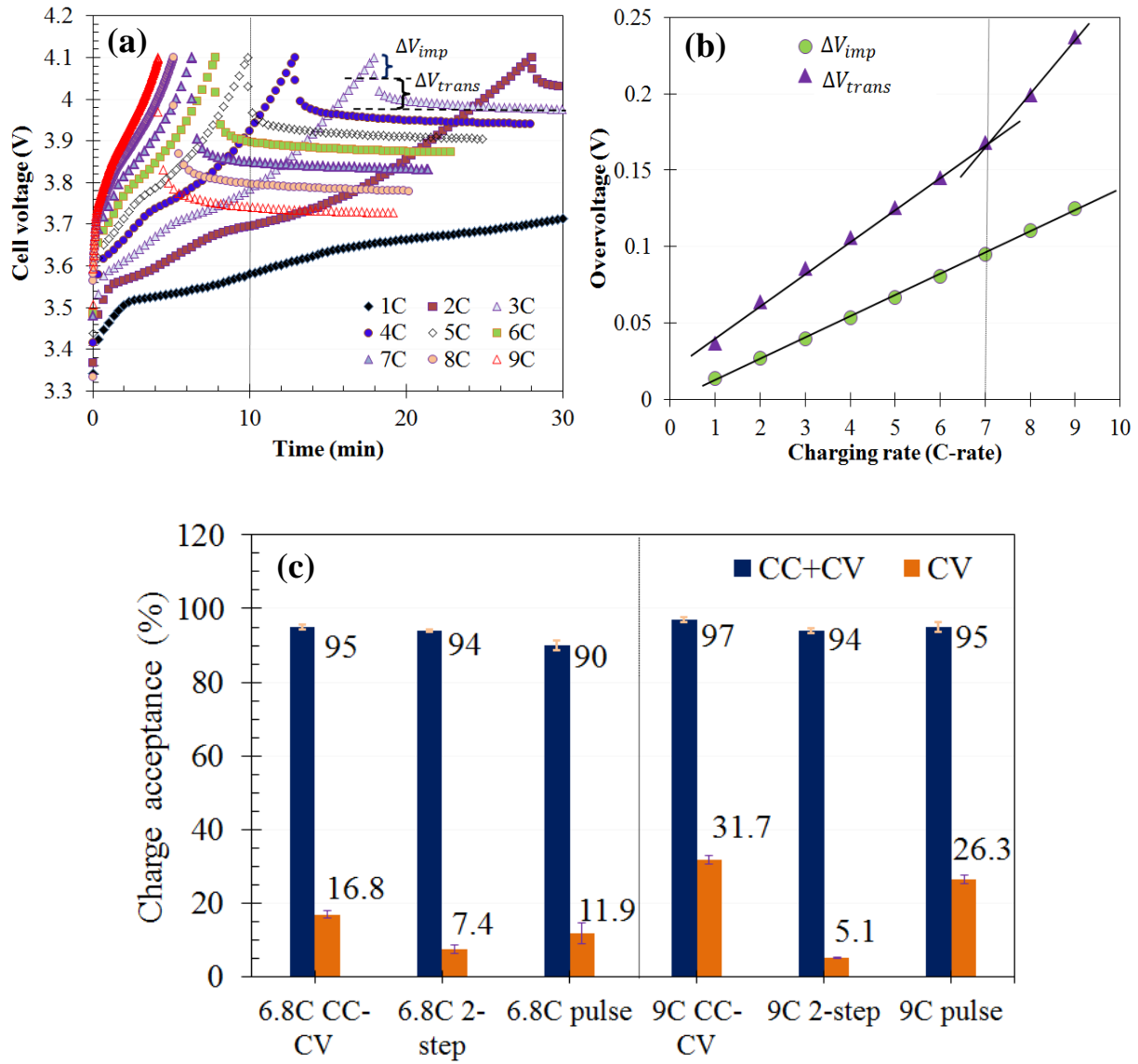


Fig. 1: (a) Voltage as a function of time during rate capability test, (b) Overtoltage components at the end of charge, and (c) Total charge acceptance at the BOL with different charging protocol and the charge acceptance during the CV portion of the charge. Note that the values shown are the average over three cells with each cell's charge acceptance scaled to the BOL C/1 capacity.

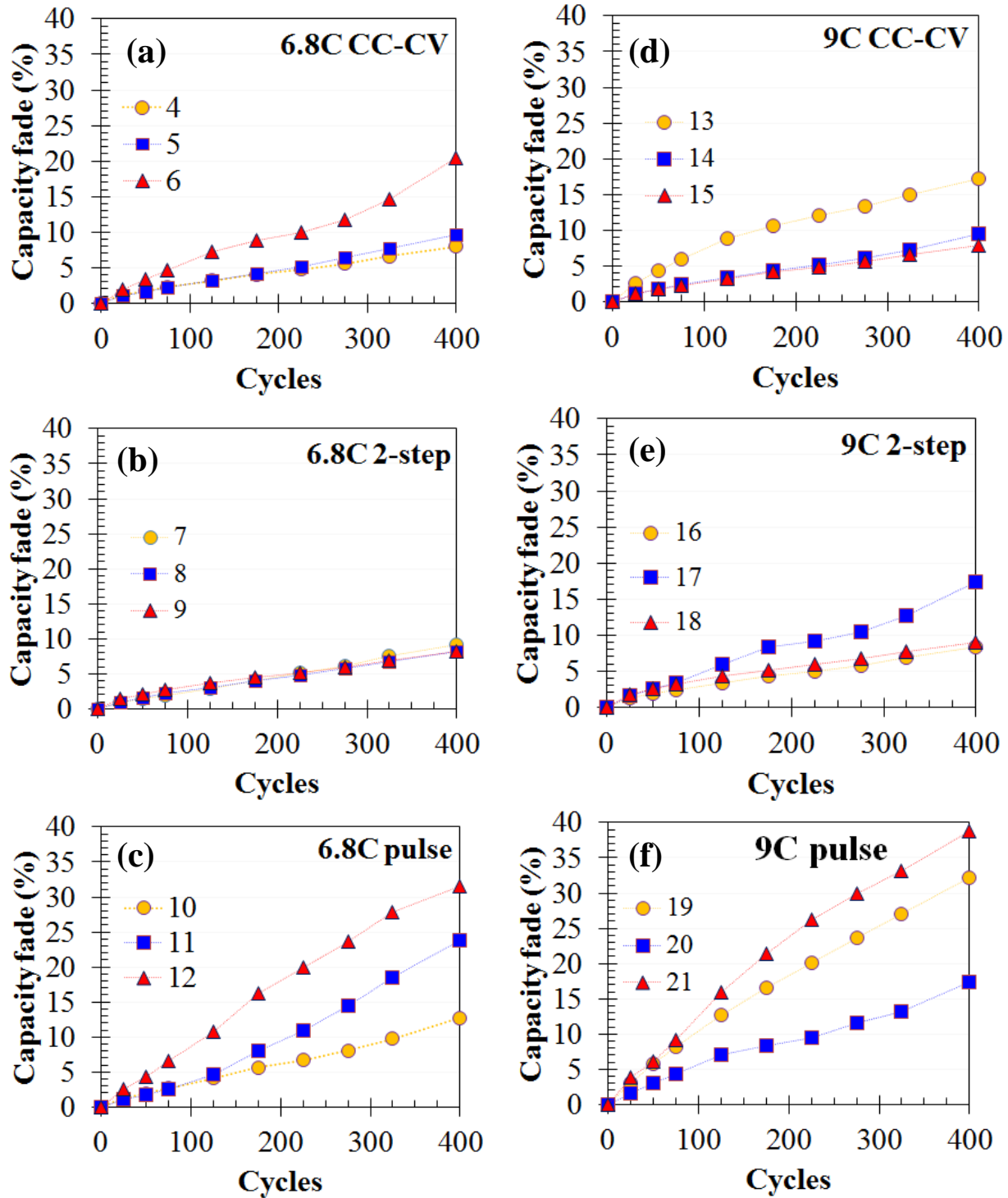


Fig. 2: C/20 capacity fades with respect to BOL capacity: (a)-(c) 6.8C charging protocols and (d)-(f) 9C charging protocols

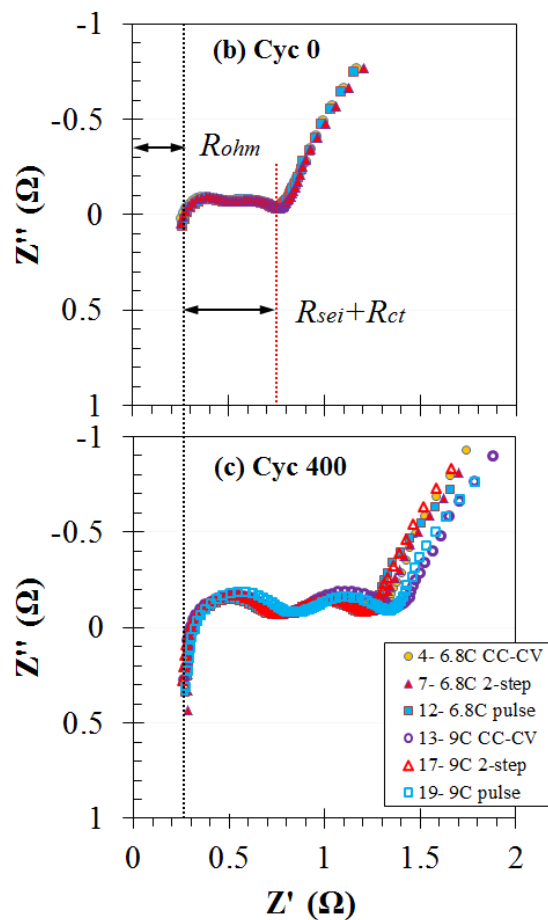
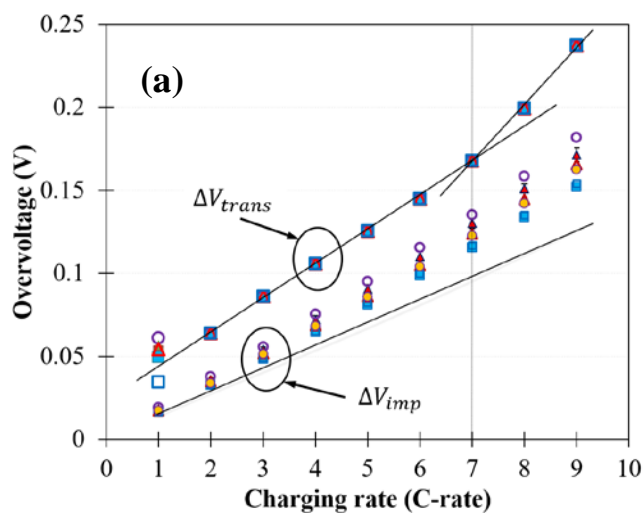


Fig. 3: Overlaid impedance and transport overvoltages at cycle 0 and 400 extracted from Fig. 1(a): cycle 0- solid lines, and cycle 400- markers, (b) EIS spectra at cycle 0 (cells 4, 5 and 6), and (c) EIS spectra at cycle 400

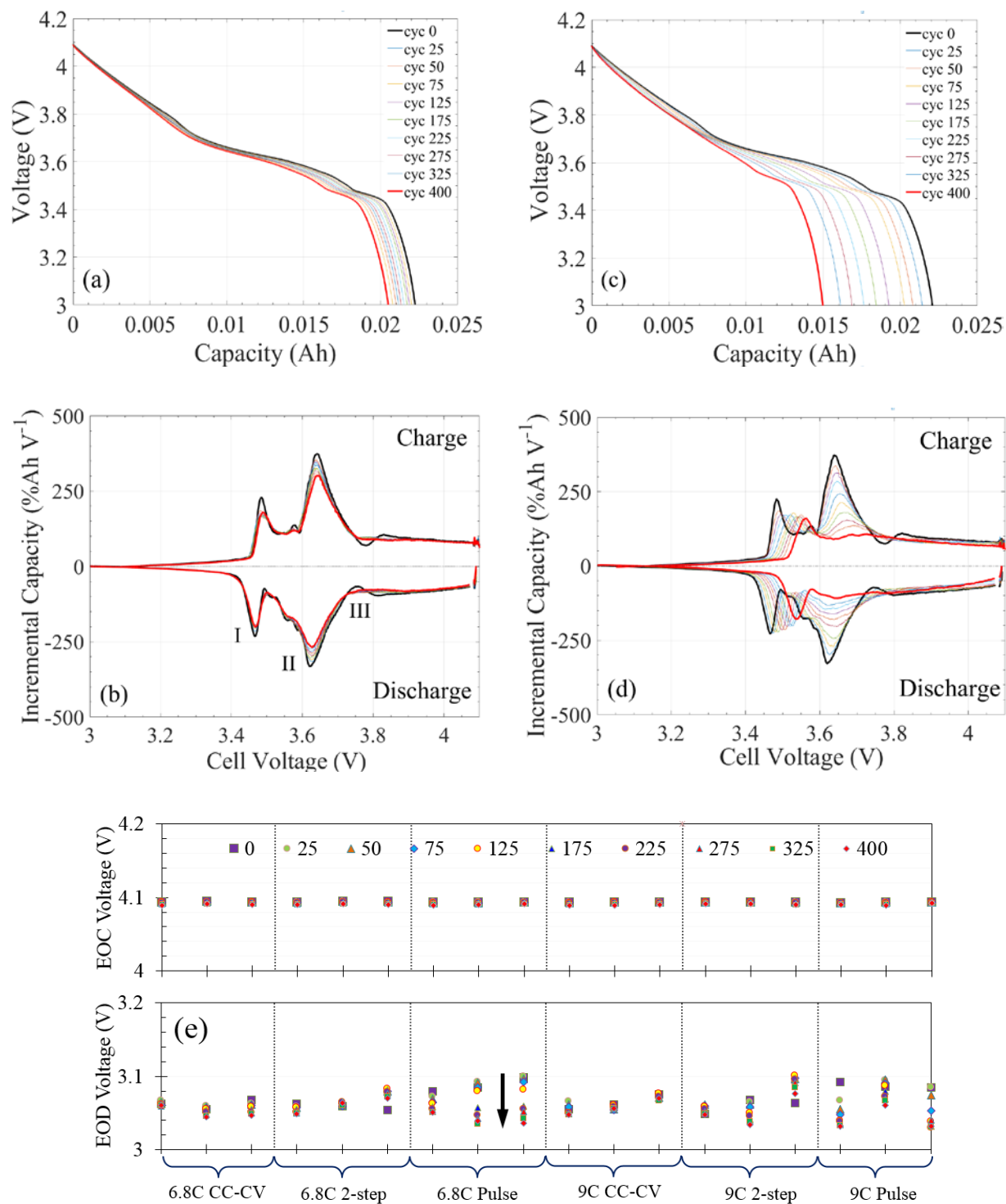


Fig. 4: (a)-(b) The lowest aged cell, cell 15- aged 8% after 400 cycles, (c)-(d) One of the highest aged cells, cell 19- aged 32% after 400 cycles, and (e) end of charge (EOC) and end of discharge (EOD) voltages. EOC and EOD voltages were collected after 1h rest followed by the end of C/20 charge and discharges, respectively. All tests were performed at C/20.

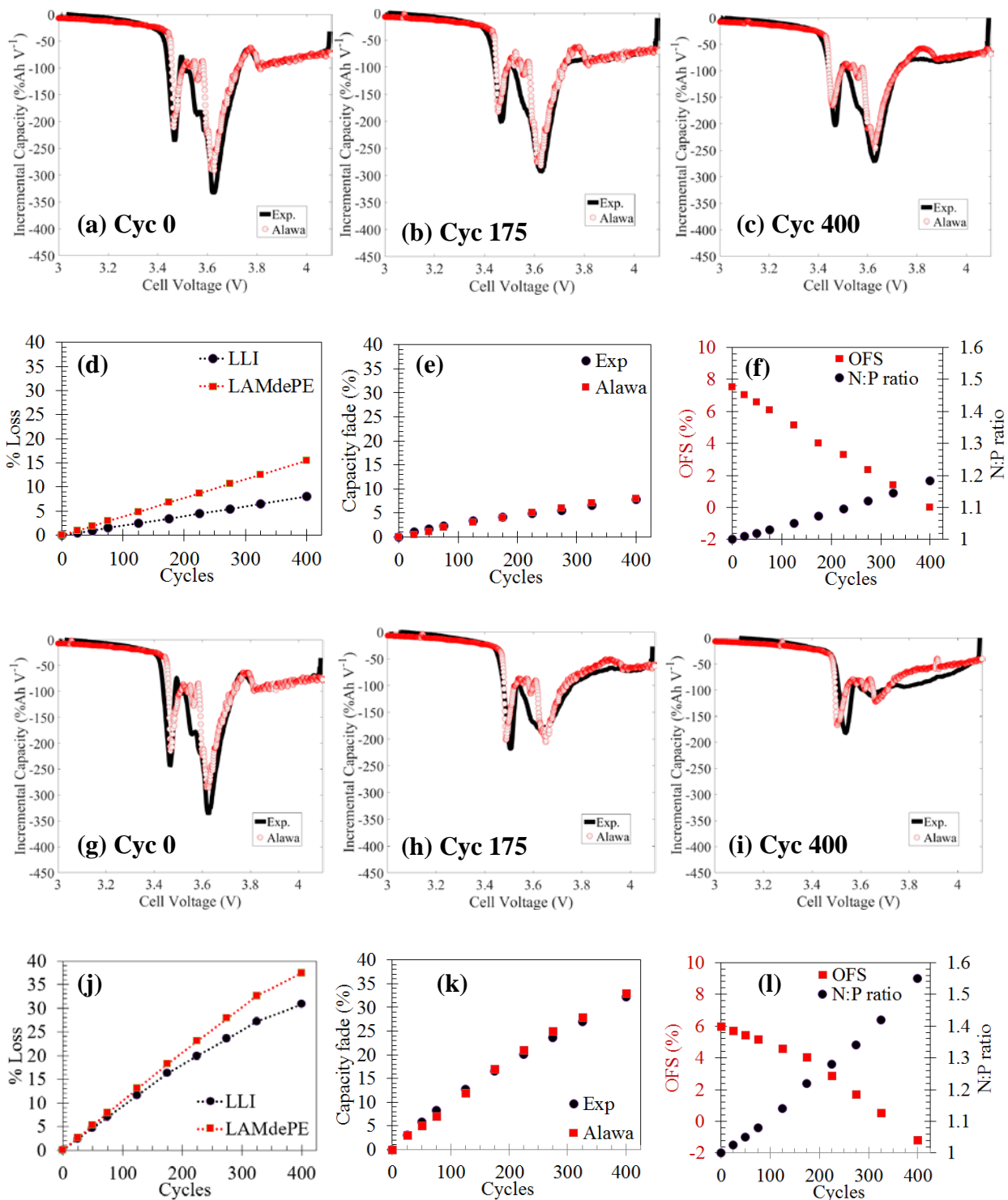


Fig. 5: (a)-(f) Comparison between experimental and Alawa $dQ.dV^{-1}$ signatures at C/20, relative aging contributions, and evolution of OFS and N:P ratio with aging for cell 15- one of the lowest aged cells, (g)-(l) Comparison between experimental and Alawa $dQ.dV^{-1}$ signatures at C/20, relative aging contributions, and evolution of OFS and N:P ratio with aging for cell 19- one of the highest aged cells.

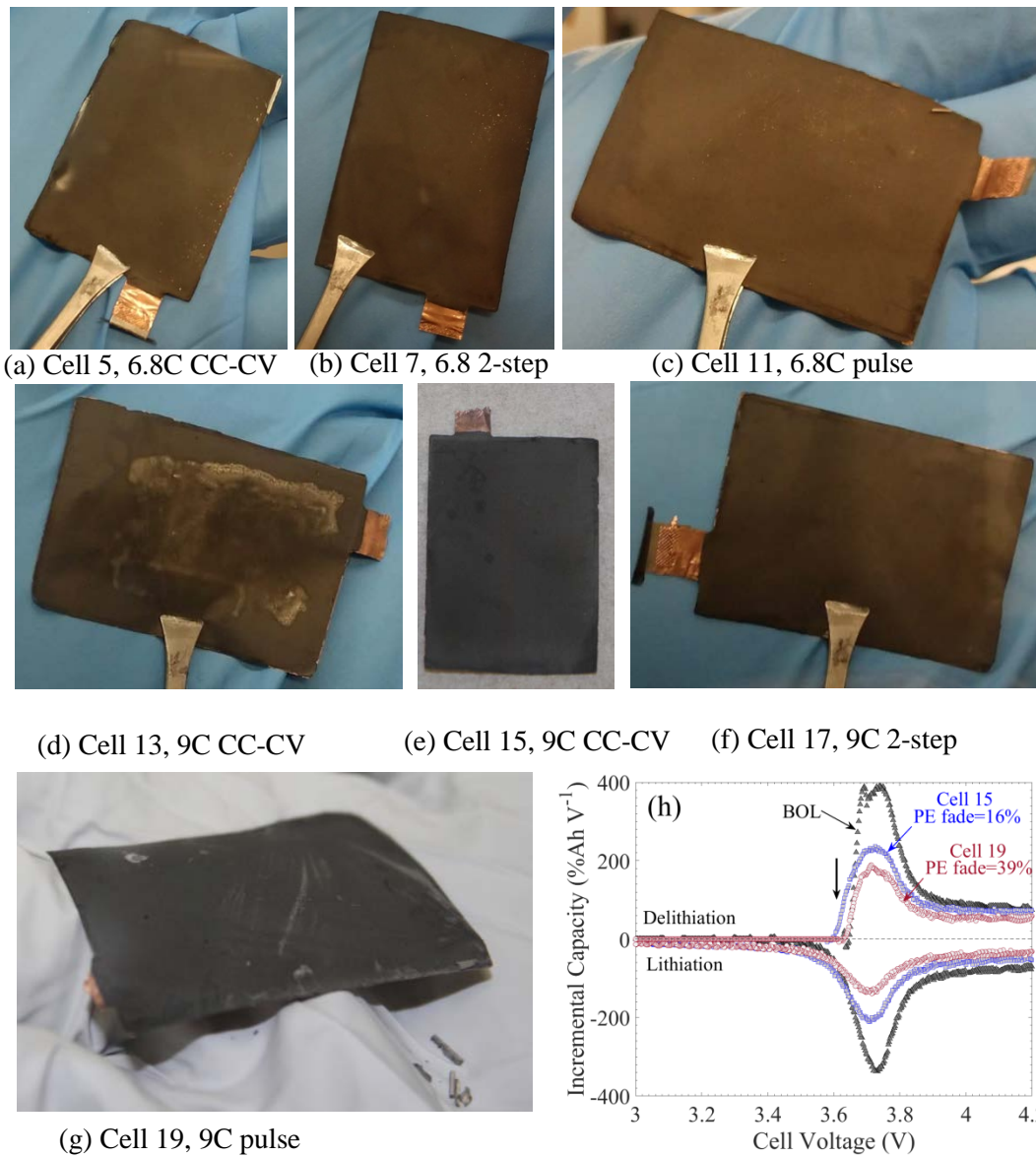


Fig. 6: (a)-(g) Teardown optical images of anodes after 400 fast charged cycles and (h) C/20 $dQ.dV^{-1}$ comparison of positive electrodes in coin cell setting (CR2032- 1.27 cm working electrode against 1.48 cm Li ref. with 1.59 cm diameter Celgard 2500 separator) harvested from cell 15 and 19. Effective C-rate remains the same in all cases.

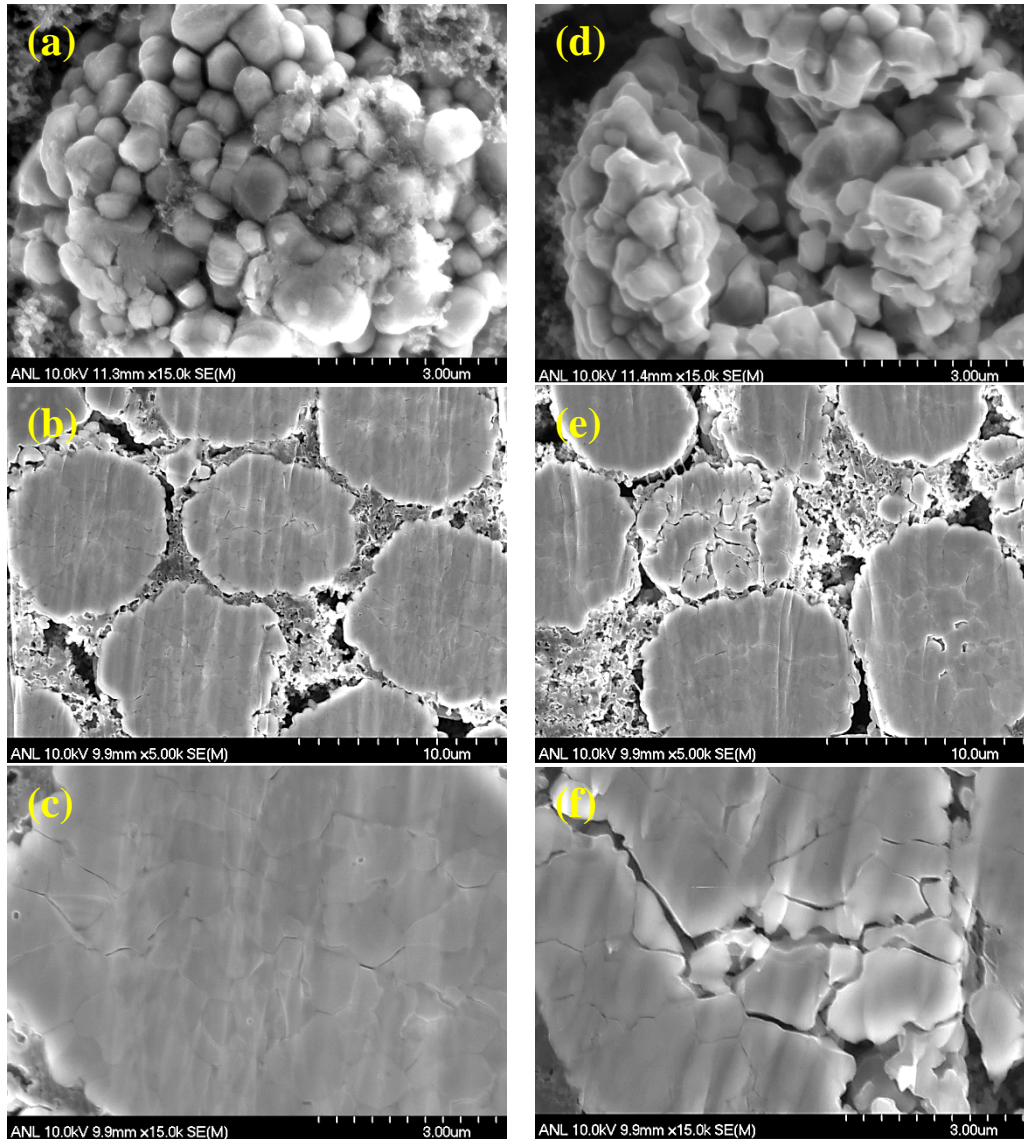


Fig. 7: Representative cell's SEM/cross sectional images: (a)-(c) SEM images of cell 7 positive electrode cycled with 6.8C 2-step protocol and (d)-(f) SEM images of cell 13 positive electrode cycled with 9C CC-CV protocol

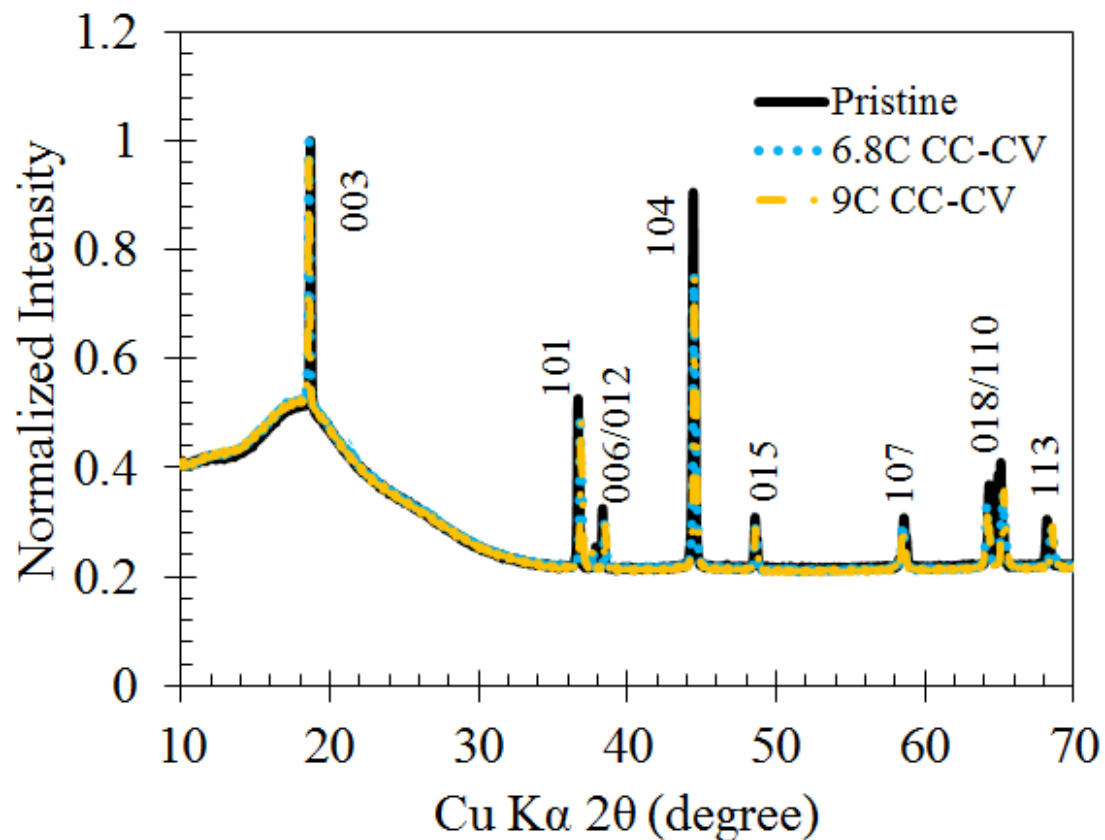


Fig. 8: XRD reflections of pristine positive electrode, cell 5 (6.8C CC-CV) and cell 13 (9C CC-CV). All intensities were normalized by pristine NMC532's peak intensity, which was 112.8 a.u.

Tables

Table I: Cell design parameters

	Negative electrode	Positive electrode
Material and composition	Superior Graphite SLC 1506T 91.83 wt % (Timcal C45 carbon 2 wt %, Kureha 9300 polyvinylidene fluoride binder 6 wt %, Oxalic acid 0.17 wt %)	Toda NMC532 90% wt % (Timcal C45 carbon 5 wt %, Solvay 5130 polyvinylidene fluoride 5 wt %)
Single side thickness with foil, μm	57	62
Foil thickness, μm	10	20
Porosity, %	37.4	33.1
Single side coating loading, mg cm^{-2}	6.38	11.4
Single side coating density, g cm^{-3}	1.36	2.71
Electrolyte	1.2 M LiPF_6 in a 3:7 by weight ethylene carbonate: ethylmethyl carbonate, 4.2x pore volume	
Separator	Celgard 2320	
Testing temperature, $^{\circ}\text{C}$	30 $^{\circ}\text{C}$	
Operating voltage $V_{\text{max}}-V_{\text{min}}$, V	4.1-3	
Formation protocol	(i) Tap charge to 1.5V and hold for 15 min, (ii) Rest at OCV for 12 h, (iii) 3 cycles at C/10, (iv) 3 cycles at C/2, and (v) Hold at 20% state of charge for 6 h	
N:P ratio	1.17 (at C/10) after formation	

Table II: Charging protocols

Charging profile	Cells (3/condition)	Initial current (C-rate)	RMS Current (C-rate)
CC-CV	4-6		
Two step CC	7-9	6.8	5.8
Pulse CC	10-12		
CC-CV	13-15		6.4
Two step CC	16-18	9	6.3
Pulse CC	19-21		6.5

Table III: Structural parameters of NMC532 at different aging states

Lattice parameters	a (Å)	c (Å)	$I_{(003)}/I_{(104)}$
Pristine NMC532	2.871	14.242 (c/a=4.96)	1.45
6.8C CC-CV (cell 5)	2.859	14.317 (c/a=5.00)	1.4
9C CC-CV (cell 13)	2.855	14.33 (c/a=5.02)	1.4